npj Clean Water

https://doi.org/10.1038/s41545-026-00581-8

Article in Press

# Cu-incorporated micro-mesoporous biochar for enhanced adsorption and persulfate-driven degradation of organic pollutants

Received: 21 March 2026

Accepted: 16 April 2026

Published online: 25 June 2026

Cite this article as: Yang, C., Lee, Y.-J., Park, S.-J. *et al.* Cu-incorporated micro-mesoporous biochar for enhanced adsorption and persulfate-driven degradation of organic pollutants. *npj Clean Water* (2026). https://doi.org/10.1038/s41545-026-00581-8

Chohee Yang, Youn-Jun Lee, Seong-Jik Park, Doyeon Lee & Eilhann E. Kwon

# Cu-incorporated micro-mesoporous biochar for enhanced adsorption and persulfate-driven degradation of organic pollutants

Chohee Yang [1], Youn-Jun Lee [1], Seong-Jik Park [2], Doyeon Lee [3, *], Eilhann E. Kwon [1, *]

[1] Department of Earth Resources and Environmental Engineering, Hanyang University, Seoul 04763, Republic of Korea; [2] Department of Bioresources and Rural System Engineering, Hankyong National University, Anseong 17579, Republic of Korea; [3] Department of Civil and Environmental Engineering, Hanbat National University, Daejeon 34158, Republic of Korea

[*]Corresponding authors: dylee82@hanbat.ac.kr (D. Lee), ek2148@hanyang.ac.kr (E.E. Kwon)



## Abstract

Integrating adsorption with heterogeneous persulfate activation represents a promising strategy for the removal of persistent organic pollutants (POPs) from aqueous systems. Nonetheless, the facile synthesis of bifunctional materials that simultaneously exhibit high adsorption capacity and strong catalytic activity remains challenging. In this study, Cu-incorporated micro/mesoporous biochar was synthesized via $CO_2$-assisted thermochemical treatment of Cu-impregnated wood chips (WC). Characterization confirmed the formation of a hierarchical micro/mesoporous structure and the presence of abundant Cu active sites in biochar (CuWCB ($CO_2$)). Performance evaluation demonstrated that CuWCB ($CO_2$) achieved a higher bisphenol A (BPA) adsorption efficiency (90.8%) than its $N_2$-derived counterpart (15.2%). Upon peroxydisulfate addition, the residual BPA was completely degraded, achieving >99% removal. In addition to its water treatment performance, the $CO_2$-assisted thermochemical treatment enhanced syngas

production. This study demonstrates an integrated strategy that couples bifunctional material synthesis with thermochemical energy recovery.

## Introduction

Persistent organic pollutants (POPs) released into aquatic environments during industrialization pose serious threats to aquatic ecosystems and human health [1]. Adsorption has been widely employed for the removal of POPs due to its operational simplicity, broad applicability, and economic viability [2, 3]. Nevertheless, the removal efficiency of POPs by adsorption is often limited by the finite number of available surface sites on the adsorbent [4]. In addition, as adsorption progresses, the concentration of pollutants in the aqueous phase decreases, thereby reducing the mass-transfer driving force for further adsorption [5]. Consequently, the system gradually approaches adsorption-desorption equilibrium, leaving residual pollutants in the treated water [6]. Thus, adsorption alone is insufficient to achieve complete pollutant removal, thereby necessitating a complementary treatment step to eliminate the remaining contaminants.

Advanced oxidation processes (AOPs) are promising technologies for water treatment because they degrade POPs through the generation of reactive oxidizing species [7]. Among AOPs, heterogeneous persulfate (PS) activation is attractive for adsorption-oxidation coupled systems because it can be readily integrated with the adsorption process, where the adsorbent also serves as a catalyst for PS activation [8]. The accumulation of pollutants on the catalyst surface also expedites removal kinetics through interfacial reactions between pollutants and oxidants [9]. Compared with conventional heterogeneous PS activation, the adsorption-oxidation process can accumulate more BPA on the catalyst surface, thereby accelerating the reaction kinetics and improving oxidant utilization [10]. As such, developing dual-function materials capable of pollutant adsorption and PS activation is of great importance.

Indeed, metal-carbon composites have attracted attention as promising materials for adsorption-oxidation integrated systems [11]. In these composites, the metal species act as active sites for PS activation, while the carbon framework provides adsorption sites for pollutant uptake [12]. In addition, the well-defined

carbon matrix promotes the dispersion of active metal species, thereby improving the accessibility of pollutants to the catalytic sites [13]. Nevertheless, the rational synthesis of metal-carbon composites remains challenging because it requires simultaneous control of carbon structure and metal dispersion [14].

Thermochemical treatment of metal-impregnated biomass offers a one-step approach for metal-carbon composite synthesis [15]. During thermochemical treatment, a carbonaceous biochar framework is formed, while the introduced metal species are deposited on the biochar surface [16]. Furthermore, metal species act as *in situ* catalysts that promote C-C/C-H bond scission in biomass-derived intermediates, thereby facilitating etching of the carbon matrix [17]. This etching process promotes the porous structure formation favorable for the transport and uptake of organic pollutants [18]. Thus, optimization of thermochemical treatment conditions is essential for engineering metal-carbon composites with accessible adsorption sites and catalytically active metal species [19].

$CO_2$-assisted thermochemical treatment offers an alternative route to conventional treatment under an inert gas condition [20]. In this process, $CO_2$ acts as an oxidizing agent that accelerates gasification of biomass carbon, thereby enhancing pore development [21]. The development of micro- and mesopores enhances the adsorption of pollutants by increasing the number of accessible adsorption sites and facilitating intraparticle mass transfer by diffusion [22]. Despite these advantages, studies on biochar carbon formation during $CO_2$-assisted thermochemical treatment remain underexplored. In particular, the synergistic effects of $CO_2$ and metal species have not been systematically investigated.

Cu-catalyzed, $CO_2$-assisted thermochemical treatment provides benefits for the resulting pyrogenic products: (i) enhanced carbon etching promotes pore development in biochar; (ii) Cu active sites are stabilized within the porous carbon framework; and (iii) Cu species catalyze reactions between $CO_2$ and bio-oil intermediates, redirecting the thermochemical pathway toward syngas production. In this study, Cu-impregnated wood chip (WC) was thermochemically treated under a $CO_2$ atmosphere to synthesize a bifunctional Cu-incorporated biochar (CuWCB ($CO_2$)). The structural, textural, and surface chemical

properties of the CuWCB ($CO_2$) were characterized. The adsorption and peroxydisulfate (PDS) activation performance of CuWCB ($CO_2$) was evaluated using bisphenol A (BPA) as a model organic pollutant. The mechanistic role of Cu during PDS activation was further investigated using multiple analyses. The gas products generated during the thermochemical treatment of Cu-impregnated WC were also monitored by time-resolved gas evolution measurements. In addition, the composition of the bio-oil fraction was analyzed to clarify the mechanistic pathways responsible for enhanced syngas (CO and $H_2$) production during $CO_2$-assisted thermochemical treatment.

## Results

### Characterization of biochars

The morphologies of WCB and CuWCB and the lattice fringes of Cu species were characterized using TEM and HRTEM. Compared with WCBs (Fig. 1(a,b,e,f)), CuWCBs exhibited Cu-containing nanoparticles dispersed on the carbon matrix (Fig. 1(c,d,g,h)). EDS elemental mapping of CuWCB ($CO_2$) showed the overlapping distributions of Cu and O, suggesting the presence of oxidized Cu species (Fig. 1(i)). The enriched N species in CuWCB ($CO_2$) likely originated from the nitrate in the Cu salt. CuWCB ($CO_2$) exhibited a mesoporous carbon structure, suggesting that Cu impregnation during $CO_2$ thermochemical treatment promoted pore development. The average particle size of CuWCB ($CO_2$) was 50.4 nm, which was larger than that of CuWCB ($N_2$) (26.0 nm). This result suggests that $CO_2$ promotes the growth of Cu species via carbon etching, which reduces support integrity and facilitated Cu aggregation [23, 24]. HRTEM images of CuWCB ($N_2$) and CuWCB ($CO_2$) showed an identical lattice spacing of 0.21 nm (Fig. 1(j,k)), which is assigned to the Cu (111) crystal plane [25].

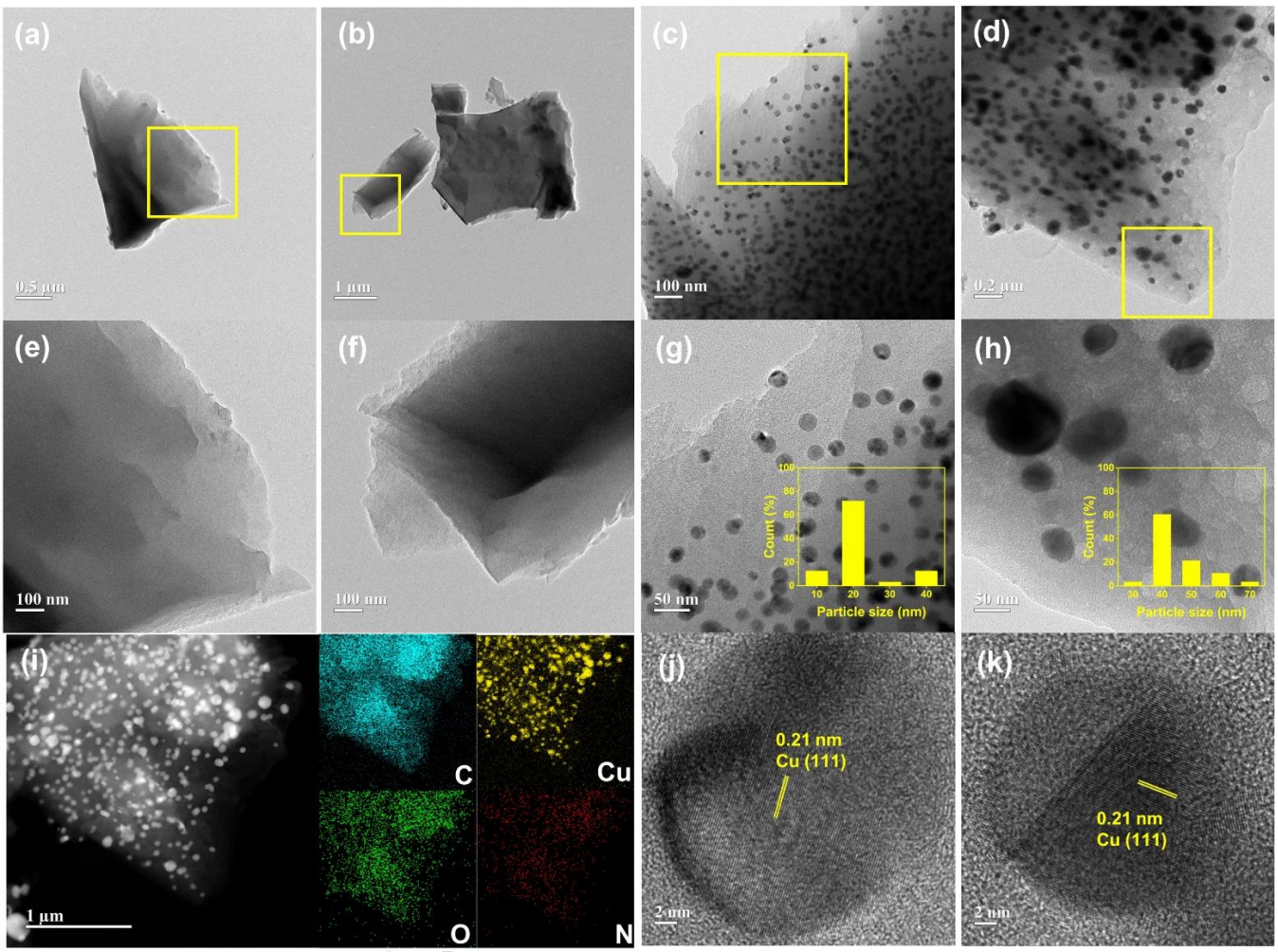


**Fig. 1 TEM, STEM, EDS, and HRTEM of WCBs and CuWCBs**. TEM images of (a,e) WCB ($N_2$), (b,f) WCB ($CO_2$), (c,g) CuWCB ($N_2$) and (d,h) CuWCB ($CO_2$). (i) STEM and corresponding EDS elemental mapping (C, O, Cu, N) of CuWCB ($CO_2$). HRTEM images of (j) CuWCB ($N_2$) and (k) CuWCB ($CO_2$).

The pore structure and surface area of WCBs and CuWCBs were characterized using $N_2$ adsorption-desorption isotherms and pore size distribution analyses. As shown in Fig. 2(a), CuWCB ($CO_2$) exhibited a higher $N_2$ uptake than the other biochars over the entire relative pressure range, indicating the presence of the most developed and accessible porosity. This result is consistent with previous studies showing that

pore development under $CO_2$ conditions is promoted in the presence of Cu species [26]. The pore size distributions (Fig. 2(b,c)) revealed that CuWCB ($CO_2$) possessed abundant micropores centered at 1.0 nm. In addition, mesopores extending to 10 nm were also observed, indicating the presence of a hierarchical micro/mesoporous framework. Quantitative results (Fig. 2(d)) demonstrated that Cu impregnation led to increases in BET surface area, BJH pore volume, and micropore volume under a $CO_2$ atmosphere. The pore structure was dominated by micropores, with a micropore volume ($V_{MP}$) of 0.24 $cm^3\ g^{-1}$, indicating that micropores constituted the majority of the accessible pore space. Meanwhile, the mesopore volume obtained from BJH analysis ($V_{BJH}$ = 0.08 $cm^3\ g^{-1}$) indicated the existence of diffusion pathways that can facilitate mass transfer of pollutants into the microporous regions [27]. In contrast, CuWCB ($N_2$) showed lower surface area and pore volume than WCB ($N_2$), suggesting that Cu impregnation under $N_2$ conditions was insufficient to develop accessible porosity. This result can be attributed to the absence of an oxidizing atmosphere and the partial blockage of pores by Cu species. Collectively, these findings indicate that pore development was governed by the synergistic effect of Cu and $CO_2$, which promoted structural rearrangement and the formation of a more accessible hierarchical pore network.

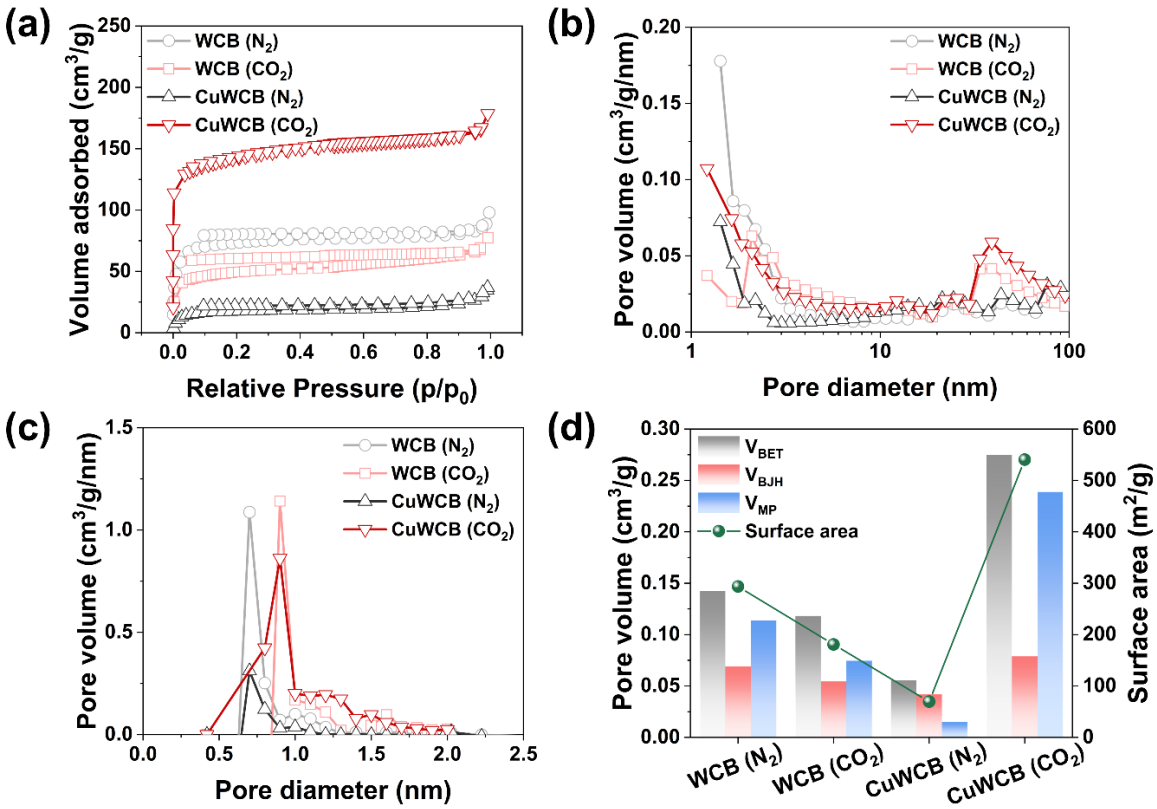


**Fig. 2 Surface area and pore structure of WCBs and CuWCBs.** (a) $N_2$ adsorption-desorption isotherms, (b) BJH pore size distributions, (c) micropore size distributions, and (d) pore volume contributions derived from BET, BJH, and micropore analyses with the BET surface areas of WCBs and CuWCBs.

As shown in Fig. 3(a), the XRD patterns verified the presence of metallic Cu phases in CuWCBs, as evidenced by the characteristic reflections at $2\theta = 43.3$, 50.5, and 74.1° (JCPDS No. 01-085-1326) [28]. The FT-IR spectra (Fig. 3(b)) showed that CuWCB ($CO_2$) retains oxygen-containing functional groups, which may facilitate BPA adsorption by providing polar interaction sites and increasing surface affinity [29]. The surface chemical states of Cu and O in the CuWCBs were characterized by XPS (Fig. 3(c-e)). The Cu $2p_{3/2}$ spectra were deconvoluted into components corresponding to $Cu^0/Cu^+$, $Cu^{2+}$, and $Cu(OH)_2$ [30]. Because $Cu^0$ and $Cu^+$ exhibit overlapping binding energies in the Cu 2p region, the Cu LMM Auger

spectra were analyzed to differentiate these Cu states [31]. The results showed that CuWCB ($CO_2$) contained a higher fraction of oxidized Cu species ($Cu^{2+}$), whereas CuWCB ($N_2$) showed a greater contribution from $Cu^0$/$Cu^+$. Consistent with this trend, the O 1s spectra revealed a higher proportion of lattice oxygen species (Cu-O) at 530.5 eV in CuWCB ($CO_2$) than in CuWCB ($N_2$) [32].

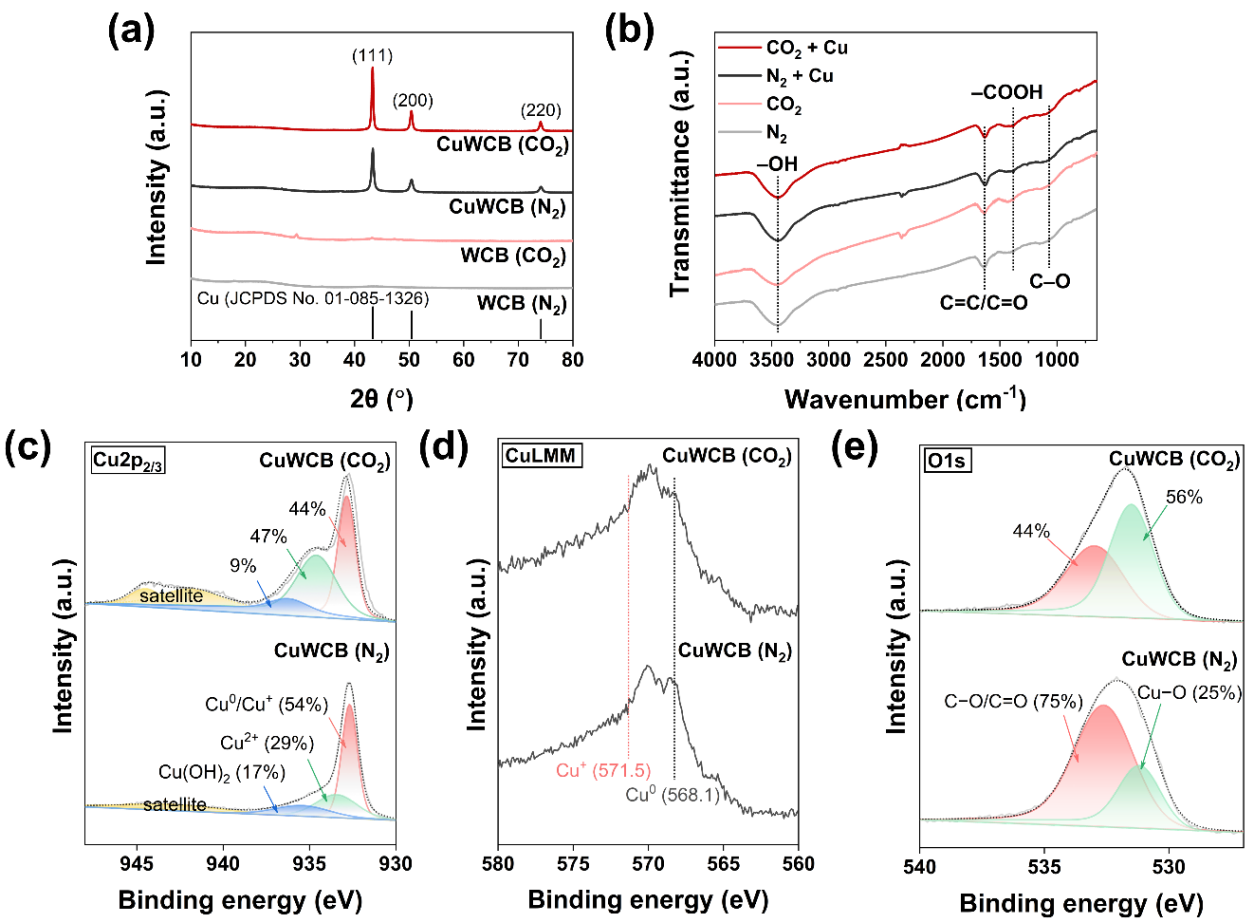


**Fig. 3 Crystal structure and surface chemical properties of WCBs and CuWCBs.** (a) XRD patterns and (b) FT-IR spectra of WCBs and CuWCBs. (c) Cu $2p_{3/2}$ XPS spectra, (d) Cu 2p LMM XPS spectra, (e) O 1s XPS spectra of CuWCB ($N_2$) and CuWCB ($CO_2$).

**Adsorption and degradation performance of BPA**

Fig. 4(a) presents the BPA removal performance during an initial adsorption stage (0-40 min), followed by PDS oxidation (40-70 min). During the adsorption stage, CuWCB ($CO_2$) showed the highest BPA removal (90.8%), exceeding that of WCB ($N_2$) (13.6%), WCB ($CO_2$) (61.2%), and CuWCB ($N_2$) (15.2%). These observations were closely associated with the hierarchical pore structure of CuWCB ($CO_2$). The microporous framework provides a large number of accessible internal adsorption sites for BPA [33]. Moreover, the mesoporous channels facilitate BPA diffusion within the biochar matrix and improve transport to these internal adsorption sites [34]. After the adsorption stage, PDS addition removed most of the residual BPA, resulting in more than 99% removal during the oxidation stage. Assessment of BPA transformation products can provide insight into the environmental safety of the treatment process. To identify the catalytic sites responsible for PDS activation, $SCN^-$ was introduced during the PDS oxidation stage as a blocker of metal active sites (Fig. 4(b)) [35]. The addition of $SCN^-$ markedly suppressed BPA degradation, reducing the removal efficiency to a level comparable to that of adsorption alone. This result indicates that PDS activation mainly occurred at Cu sites rather than on the biochar matrix [35]. The roles of reactive oxygen species in BPA degradation during the oxidation stage were further examined using scavenger tests (Fig. 4(c)). The scavenger concentrations were selected based on previous studies [36, 37, 38]. The addition of MeOH, CF, and SA did not decrease BPA removal during PDS oxidation, suggesting that •OH/ $SO_4^{\bullet-}$, $O_2^{\bullet-}$,and $^1O_2$ played a minor role in the degradation of BPA [39]. Consistent with the scavenger test results, EPR analysis showed no distinct signal corresponding to $^1O_2$. Moreover, the low conversion efficiency of BA to 4-HBA ($\eta_{4\text{-HBA}} = 0.48\%$), compared with that reported for •OH-dominant systems (> 5%), indicates that •OH did not play a major role in BPA degradation [40].

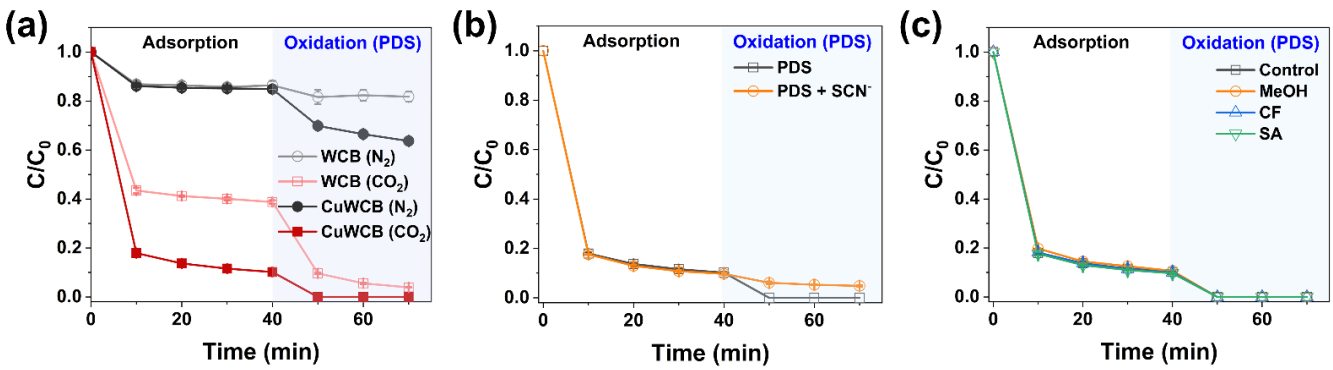


**Fig. 4 BPA removal performance of WCBs and CuWCBs and mechanistic evaluation of PDS oxidation over CuWCB ($CO_2$).** (a) BPA removal test of WCBs and CuWCBs including adsorption and PDS oxidation. (b) Effect of $SCN^-$ (1 mM) and (c) scavengers (MeOH = 100 mM, CF, and SA = 1 mM) on BPA degradation during PDS oxidation over CuWCB ($CO_2$) (catalyst dose = 0.4 g/L, $[BPA]_0$ = 70 μM, $[PDS]_0$ = 1 mM).

**Catalytic mechanism for PDS activation**

Electrochemical impedance spectroscopy (EIS) was employed to compare the interfacial charge-transfer resistance of WCBs and CuWCBs (Fig. 5(a)). Cu incorporation decreased the imaginary impedance component (-Z''), suggesting reduced interfacial polarization [41]. The smaller semicircle observed in the high-frequency region for the $CO_2$-derived biochars indicates lower charge-transfer resistance at the catalyst-electrolyte interface [42]. Among biochars, CuWCB ($CO_2$) exhibited the smallest semicircle diameter, consistent with the lowest charge-transfer resistance and more favorable interfacial electron-transfer kinetics [43]. This improved electrochemical response is consistent with its hierarchical micro-mesoporous structure, which promotes electrolyte diffusion into the porous framework.

Open circuit potential (OCP) and chronoamperometry (CA) were conducted to elucidate the interfacial behavior of PDS on the CuWCB ($CO_2$) surface. As shown in Fig. 5(b), the OCP increased to 0.8 V (vs Ag/AgCl) following PDS addition, indicating oxidative polarization of the catalyst surface and the formation of a surface-bound CuWCB ($CO_2$)/PDS complex [44]. Upon subsequent BPA addition, the OCP decreased, consistent with interfacial electron donation from the BPA to the activated CuWCB($CO_2$)/PDS complex [45]. This result suggests that electron transfer driven by the interfacial redox potential facilitated PDS decomposition and initiated the oxidation of BPA. Density functional theory (DFT) calculations can be included in a follow-up study to elucidate the electronic interactions between Cu sites and PDS during activation. This interpretation was further supported by CA (Fig. 5(c)). Upon PDS addition, the cathodic current increased in magnitude, reflecting electron density redistribution associated with PDS adsorption/activation [46]. This indicates the formation of surface-bound Cu/PDS complex and oxidation of Cu species. Subsequent BPA addition induced a current transient, suggesting accelerated interfacial electron transfer accompanied by consumption of the activated oxidant complex during BPA oxidation [47].

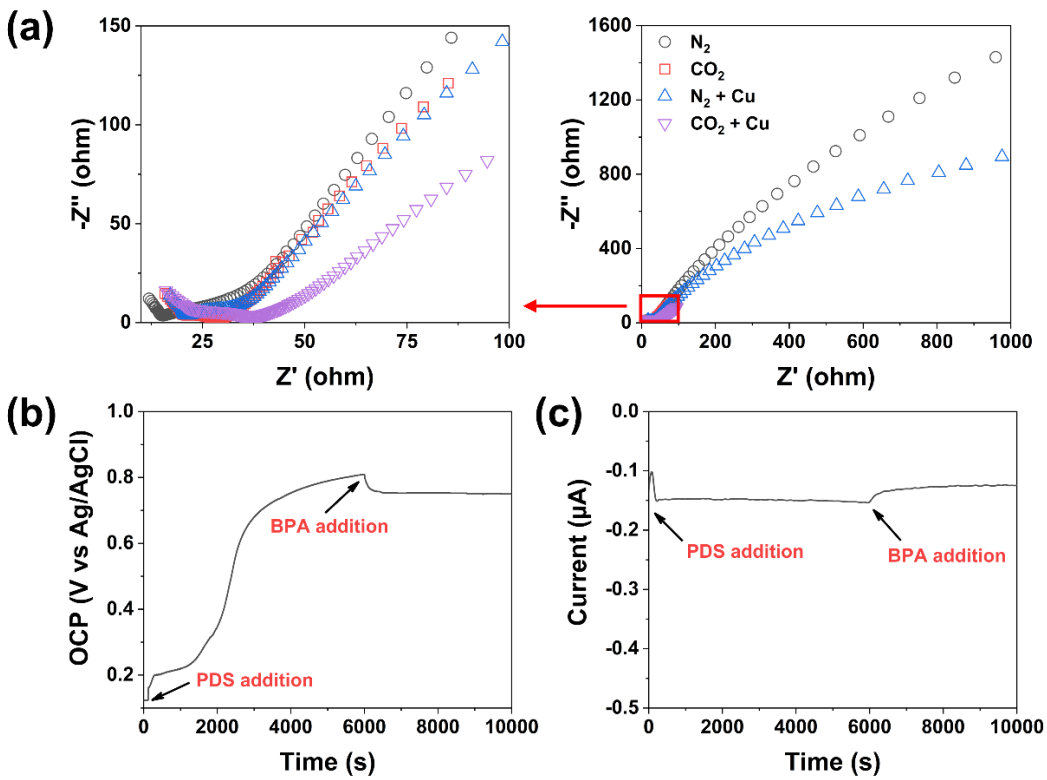


**Fig. 5 Electrochemical properties of WCBs and CuWCBs.** (a) Electrochemical impedance spectroscopy (EIS) of WCBs and CuWCBs. (b) Open circuit potential (OCP) and (c) chronoamperometry (CA) measurements of CuWCB ($CO_2$) upon PDS and BPA addition ($[BPA]_0$ = 25 μM, $[PDS]_0$ = 500 μM).

The Cu $2p_{3/2}$ and Cu LMM Auger XPS spectra of CuWCB ($CO_2$) were analyzed before and after reaction to elucidate the evolution of surface Cu species during oxidant activation. In the Cu $2p_{3/2}$ region, CuWCB ($CO_2$) after reaction exhibited an increased contribution from Cu(II) accompanied by a decreased $Cu^0/Cu^+$ fraction, suggesting oxidation of Cu species during PDS activation (Fig. 6(a)). The Cu LMM Auger spectra showed a shift in the Cu speciation from a $Cu^0$-rich surface toward a $Cu^+$-dominated state (Fig. 6(b)), indicating the oxidation of surface Cu during the reaction. This result indicates that Cu active sites served as the primary sites for PDS activation through electron donation. Based on the mechanistic

investigations, the adsorption and PDS activation mechanisms for BPA removal over CuWCB ($CO_2$) are illustrated in Fig. 7 [48, 49, 50]. BPA removal was governed by adsorption on the CuWCB ($CO_2$) and oxidation through the Cu/PDS complex.

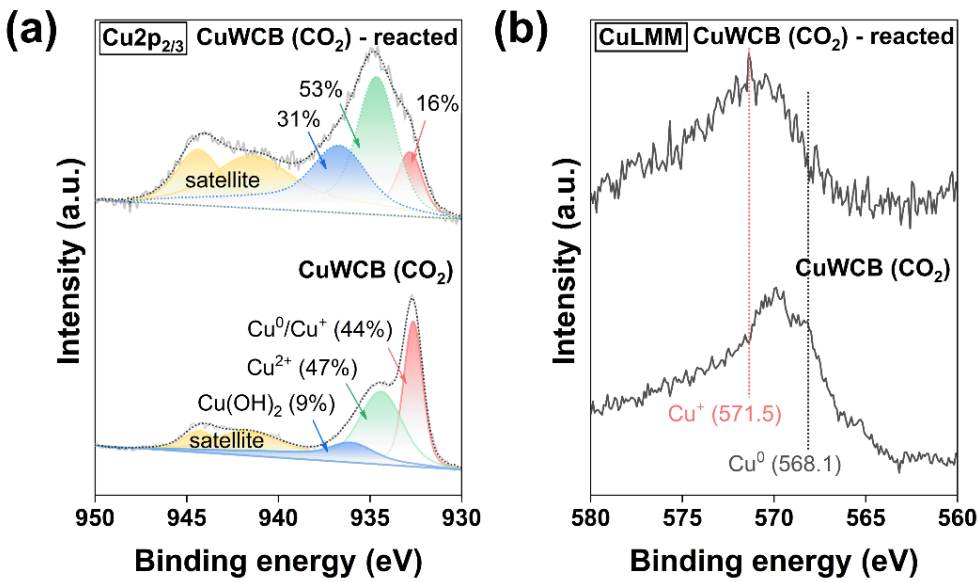


**Fig. 6 Cu XPS analysis of CuWCB ($CO_2$) before and after reaction.** (a) Cu $2p_{3/2}$ and (b) Cu LMM Auger XPS spectra of CuWCB ($CO_2$) before and after reaction.

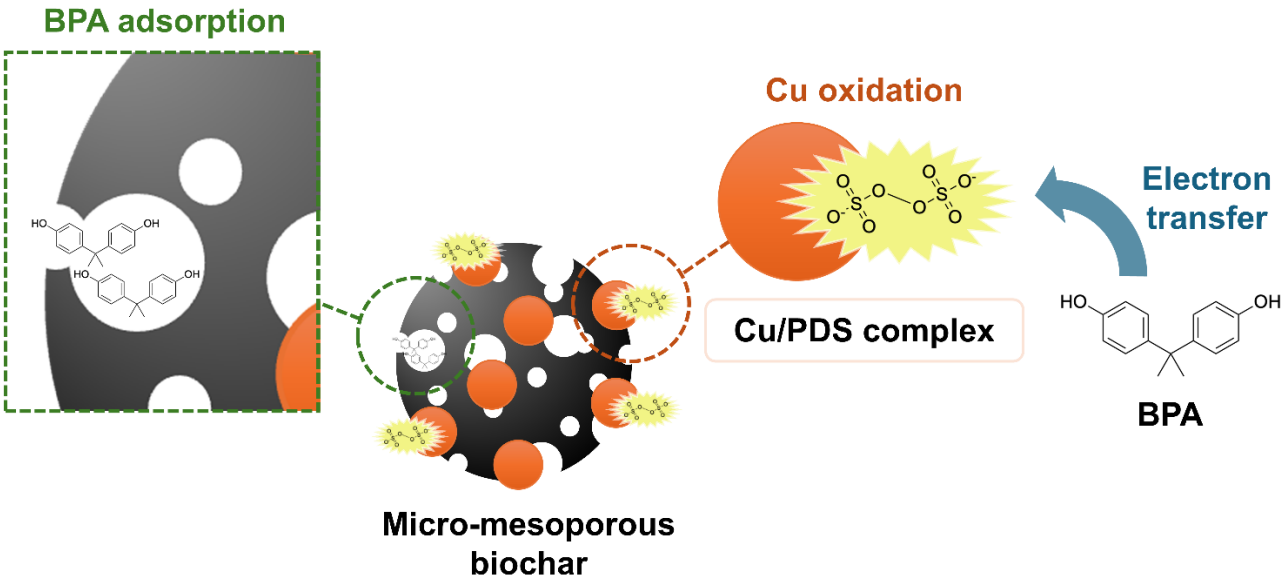


**Fig. 7 Adsorption-PDS oxidation mechanism over CuWCB ($CO_2$).** Schematic diagram of adsorption-PDS oxidation mechanism over CuWCB ($CO_2$).

**Catalyst durability and matrix tolerance**

To evaluate the reusability of the catalyst, cyclic BPA removal tests were conducted [51]. CuWCB ($CO_2$) maintained high BPA removal performance over the first three cycles, but its removal efficiency decreased in the fourth cycle (Fig. S2). This decrease was likely associated with the accumulation of adsorbed BPA on the catalyst surface, which hinders the access of dissolved BPA and PDS to the active Cu sites. To examine the structural stability of the catalyst after repeated use, the spent catalyst was characterized by XRD and XPS analyses. The XRD patterns showed that the characteristic diffraction peaks of $Cu^0$ were preserved after five cycles (Fig. S3). XPS analysis of the Cu $2p_{3/2}$ region showed that no new peaks emerged after the 5-cycle test (Fig. S4). Changes were observed only in the relative fractions of the components. The O 1s and C 1s spectra also showed no significant changes in the identified components, except for variations in their relative fractions. The negligible leaching of Cu ions into the reaction solution supports the structural stability of the catalyst during repeated use (Fig. S5).

The effects of background constituents (humic acid, $Cl^-$, and $HCO_3^-$) on BPA removal were investigated. During the adsorption stage, the presence of background constituents caused a slight decrease in BPA adsorption. After the addition of PDS, BPA was completely removed within 10 min under all conditions. These results suggest the robustness of CuWCB ($CO_2$) in complex water matrices.

**Thermochemical treatment of WC**

The thermogravimetric behavior of WC and CuWC was evaluated under $N_2$ and $CO_2$ atmospheres using TG and DTG analyses (Fig. 8). Pristine WC exhibited two major mass-loss events at 285 ˚C and 355 ˚C, which can be attributed to the thermal decomposition of hemicellulose and cellulose, respectively [52]. Under a $CO_2$ atmosphere, WC showed an additional high-temperature mass-loss feature above 650 ˚C relative to $N_2$. This mass loss is ascribed to $CO_2$-carbon gasification via the Boudouard reaction ($CO_2 + C \rightarrow 2CO$), indicating a heterogeneous gas-solid reaction between $CO_2$ and the carbonaceous matrix. Notably, Cu impregnation lowered the onset temperature of this gasification feature to ~620 ˚C, suggesting that Cu promotes biochar carbon gasification.

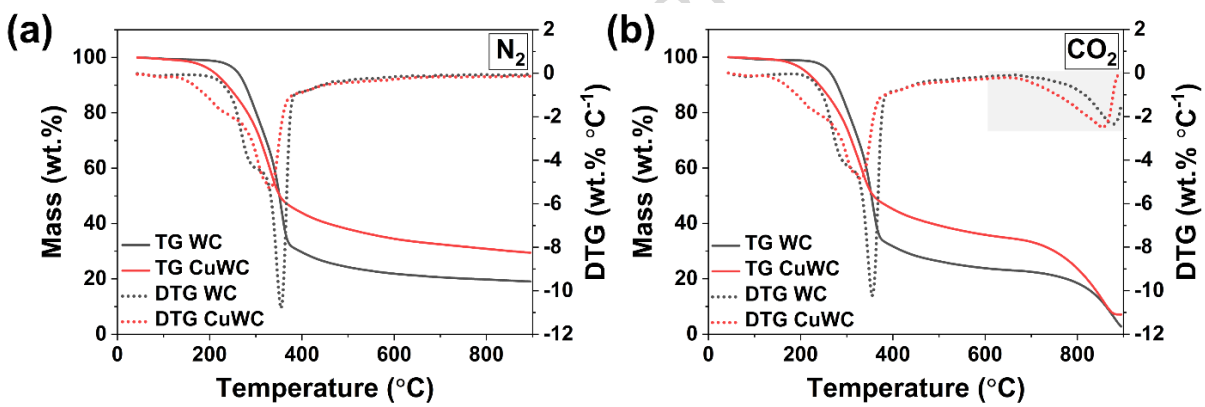


**Fig. 8 Thermal decomposition behavior of WC and CuWC.** TGA and DTG profiles of WC and CuWC under (a) $N_2$ and (b) $CO_2$ atmospheres.

Time-resolved concentration profiles of the gaseous products (CO, $H_2$, $CH_4$, and $C_2$-hydrocarbons ($C_2$ HCs)) generated during thermochemical processing under $N_2$ and $CO_2$ atmospheres are presented in Fig. 9. The $N_2$ and $CO_2$ atmospheres exhibited no significant differences in CO and $H_2$ evolution at temperatures below 550 ˚C. In contrast, CO formation under $CO_2$ increased markedly above 550 ˚C, accompanied by a simultaneous decrease in $H_2$ concentration. This inverse relationship indicates the

occurrence of the reverse water-gas shift reaction ($CO_2 + H_2 \rightarrow CO + H_2O$), in which $H_2$ is consumed to promote CO formation under $CO_2$ atmosphere [53]. Notably, the CO increase exceeded the decrease in $H_2$, suggesting additional CO formation via homogeneous $CO_2$-volatile reactions [21]. Moreover, CO generation accelerated above 650 ˚C via the Boudouard reaction, consistent with the trends observed in the TGA/DTG profiles. After Cu impregnation, the CO yield increased under $CO_2$ and the onset temperature for CO evolution decreased, indicating Cu-catalyzed gasification of biochar carbon. The increased CO production indicates more extensive carbon etching in CuWCB ($CO_2$), which is consistent with the enhanced pore development. In the 200-550 ˚C range, formation of $CH_4$ and $C_2$ HCs was suppressed, whereas $H_2$ evolution was enhanced, implying that Cu promotes dehydration/condensation of volatile intermediates during primary devolatilization and favors their incorporation into the solid carbon matrix [54]. This interpretation is supported by TGA results, which show a higher char residue for CuWC (37.3%) than for pristine WC (24.9%) at 550 ˚C under a $CO_2$ atmosphere.

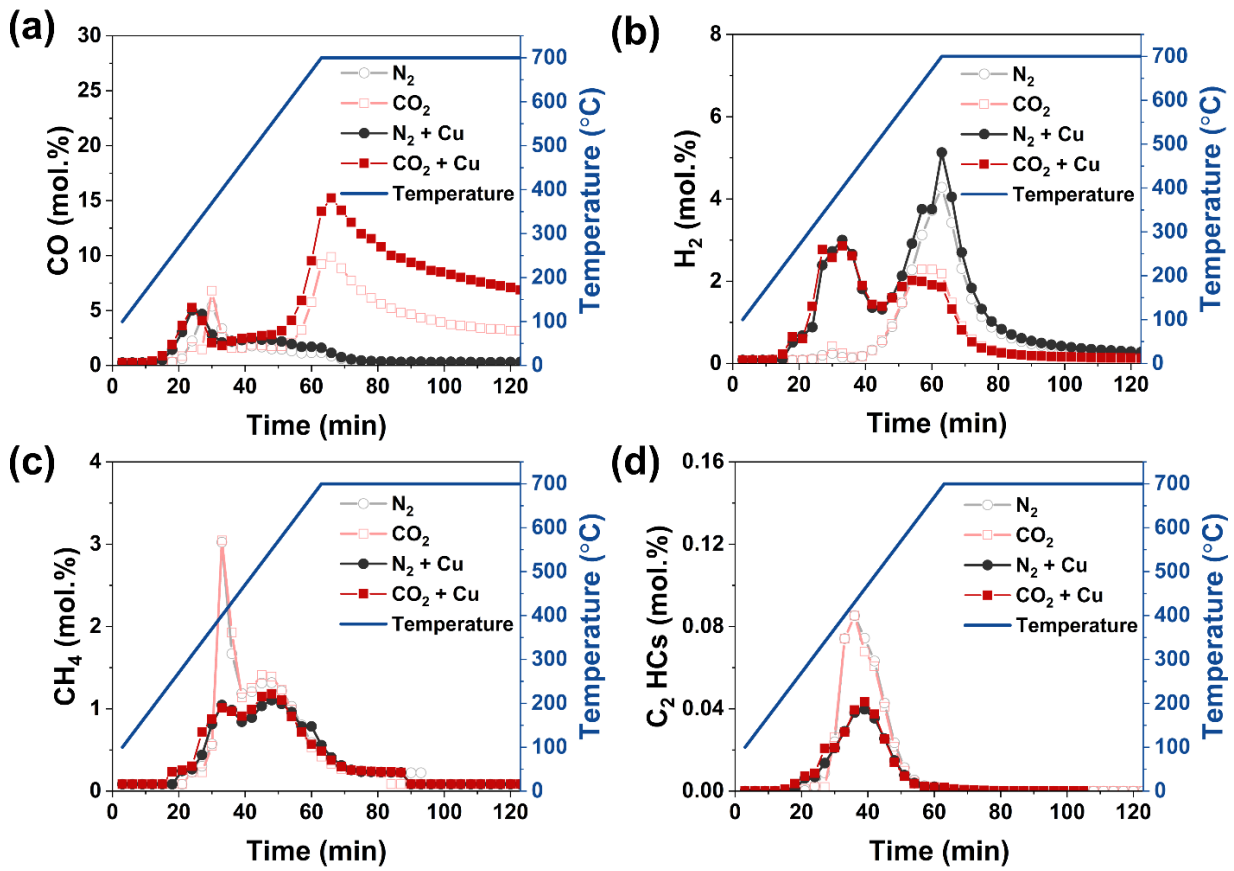


**Fig. 9 Gas evolution profiles during the thermochemical process.** Time-resolved concentration profiles of gaseous products during the pristine/Cu-doped WC thermochemical process under $N_2/CO_2$ atmosphere: (a) CO, (b) $H_2$, (c) $CH_4$, and (d) $C_2$ HCs.

The corresponding mass distribution of gas, liquid, and solid products is presented in Fig. 10 (a). Under $CO_2$ atmosphere, Cu impregnation increased the gas yield from 35% to 49%. Cumulative gas yield during the temperature-ramping and isothermal stages was calculated to quantitatively compare gas evolution (Fig. 10(b-d)). After Cu impregnation, the yields of $CH_4$ and $C_2$ HCs decreased by 19% and 43%, respectively, whereas the $H_2$ yield increased by 35% during the temperature-ramping stage. Moreover, CO production increased by 31%, indicating enhanced *in situ* syngas upgrading catalyzed by Cu. As a result, during the temperature-ramping stage of CuWC, CO and $H_2$ production reached 35.1 and 16.1

mmol, respectively, under $CO_2$. During the isothermal stage under $CO_2$ atmosphere, CO production increased from 50.1 to 101.8 mmol after Cu impregnation, corresponding to a 2.03-fold increase. Consequently, CO and $H_2$ together accounted for 94% of the total gas products during the overall $CO_2$-assisted thermochemical process, which was higher than the corresponding values for WC ($N_2$) (77%), CuWC ($N_2$) (85%), and WC ($CO_2$) (88%).

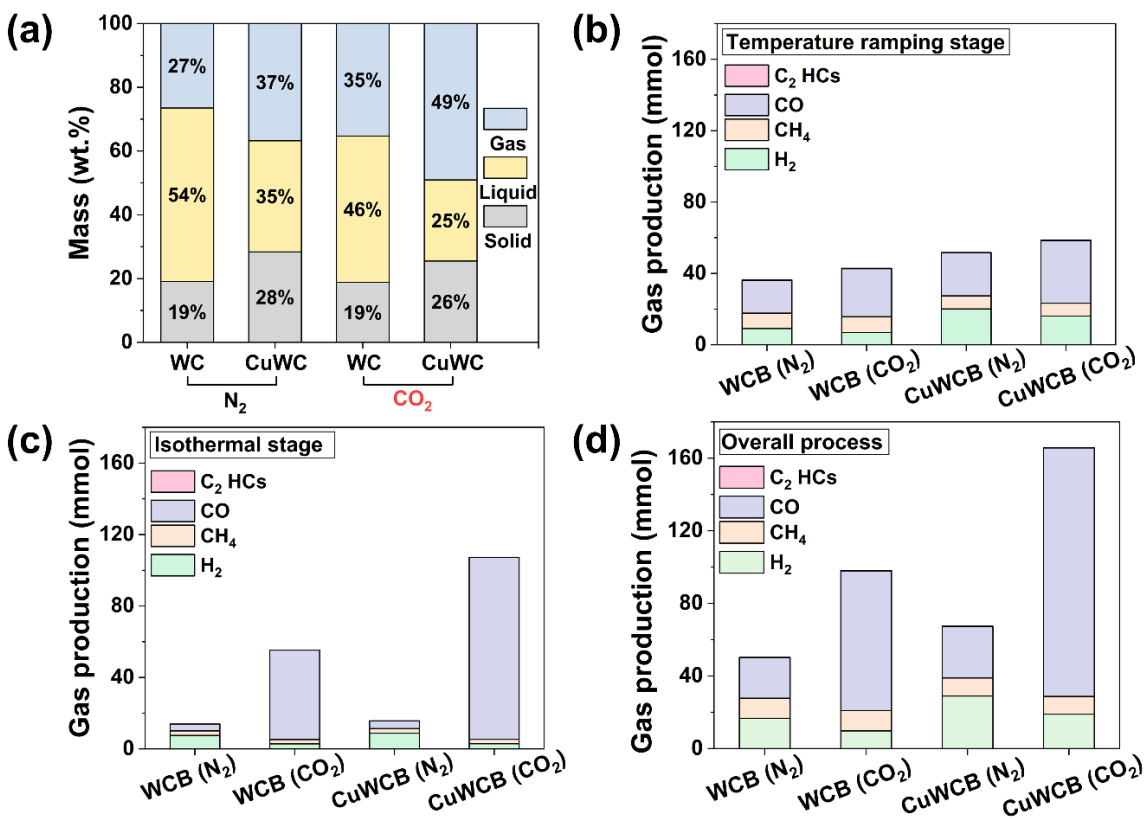


**Fig. 10 Product distribution and cumulative gas yield.** (a) Mass distribution of gas, liquid, and solid products. Cumulative gas yield during the (b) temperature-ramping, (c) isothermal stages, and (d) overall thermochemical process.

**Thermochemical process mechanism**

The liquid products from the WC thermochemical process were analyzed using a GC-MS. The chromatograms of WC and CuWC under $N_2$ and $CO_2$ are presented in Fig. 11(a). The identification results

and peak areas of bio-oil compounds were summarized across the different conditions (Table S1). Relative to pristine WC, Cu impregnation markedly attenuated the intensities of the major compounds. This indicates that Cu catalyzed the conversion of condensable oxygenated intermediates into gas products, consistent with the decrease in liquid yield from 46% to 25% (Fig. 10(a)).

Identified oxygenated compounds in the bio-oil were categorized into five groups: acids, ketones, furans, phenolics, and others, and the corresponding cumulative peak areas are presented in Fig. 11(b). These oxygenated species originate from lignocellulosic thermolysis: acids, ketones, and furans are primarily generated from (hemi)cellulose decomposition [55], whereas phenolics originate from lignin degradation due to its complex aromatic structure [56]. Switching from $N_2$ to $CO_2$ reduced the cumulative peak areas for all compound classes, and Cu impregnation further amplified this reduction. Specifically, the total peak areas of oxygenated compounds under $CO_2$ in the presence of Cu decreased by 62% relative to pristine WC. Because the oxygen-rich and chemically complex composition of bio-oils limits their direct use as fuels [57], converting these intermediates to syngas enables more efficient energy utilization. Overall, the Cu-catalyzed $CO_2$-assisted thermochemical processing redirects reaction pathways toward syngas production and depletes oxygenated intermediates.

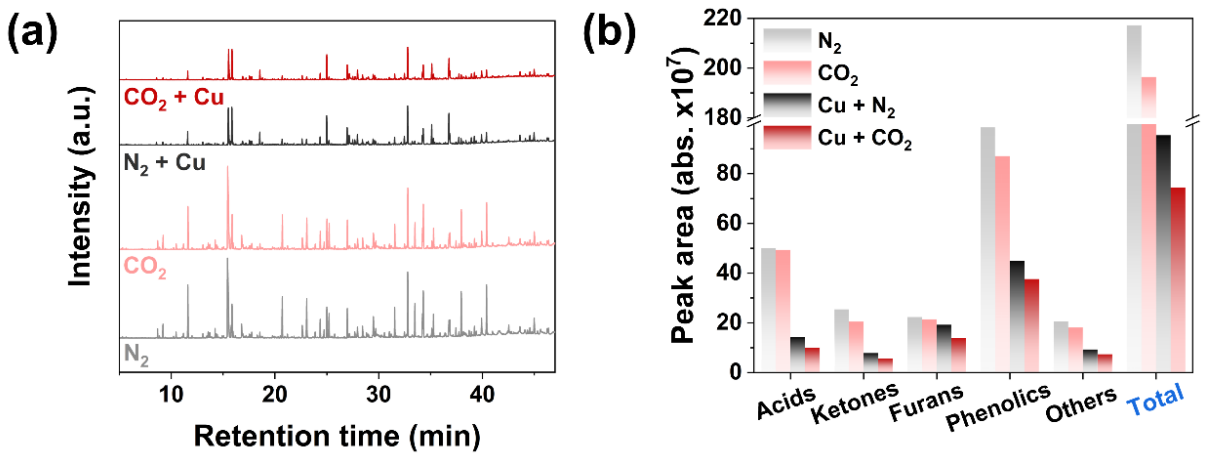


**Fig. 11 Chemical composition of bio-oil.** (a) GC-MS chromatograms and (b) cumulative peak areas of oxygenated compounds in bio-oil products obtained from thermochemical process of WC/CuWC under $N_2/CO_2$ atmospheres.

## Discussion

In this study, Cu-impregnated WC was thermochemically treated under a $CO_2$ atmosphere to synthesize a Cu-biochar composite for adsorption-oxidation applications. The Cu-$CO_2$ synergy during thermochemical treatment led to the formation of a hierarchical micro/mesoporous structure in CuWCB ($CO_2$), thereby enhancing BPA adsorption (90.8 % of BPA removed). The residual BPA after adsorption was subsequently removed through PDS activation by Cu active species, resulting in a total removal efficiency of >99%. Beyond catalytic performance, the Cu-catalyzed $CO_2$-assisted thermochemical treatment redirected WC decomposition toward syngas formation while suppressing the formation of oxygenated liquid intermediates. The CO yield reached 136.9 mmol, and syngas (CO + $H_2$) accounted for 94% of the total gas products, exceeding the corresponding values for CuWC ($N_2$) (85%) and WC ($CO_2$) (88%). These results provide a mechanistic basis for understanding the role of transition metal species in pyrogenic product evolution during $CO_2$-assisted thermochemical treatment. Overall, this study demonstrates a practical approach that integrates $CO_2$-assisted thermochemical energy recovery with the synthesis of functional materials for water treatment systems.

## Methods

### Materials and chemicals

WC was purchased from a landscaping supplier in South Korea. Bisphenol A (BPA, $C_{15}H_{16}O_2$, > 99%), potassium bromide (KBr, > 99%), sodium thiocyanate (NaSCN, > 98%), and sodium azide (SA, $NaN_3$, > 99.5%) were supplied by Sigma-Aldrich (USA). Copper(II) nitrate trihydrate ($Cu(NO_3)_2 \cdot 3H_2O$, guaranteed reagent grade) and sodium peroxydisulfate ($Na_2S_2O_8$) were obtained from Junsei Chemical (Japan). Acetonitrile (ACN, $CH_3CN$, HPLC grade), chloroform (CF, $CHCl_3$, HPLC grade), methanol (MeOH, $CH_3OH$, HPLC grade), and dichloromethane (DCM, $CH_2Cl_2$, > 99.9%) were purchased from Daejung Chemicals & Metals (South Korea). A certified calibration gas standard containing $N_2$, $CO_2$, $H_2$, CO, $CH_4$, $C_2H_6$, $C_2H_4$, and $C_2H_2$ was provided by RIGAS (South Korea). Ultra-high-purity $N_2$ and $CO_2$ gases were supplied by Green Gas (South Korea).

### Biochar synthesis

WC was dried in oven (95 ˚C) for 24 h to eliminate residual water content, then ground and sieved to collect < 600 μm particle fractions. Cu-impregnated WC was prepared using wet impregnation by targeting a Cu loading of 5.00 wt.% based on the dry biomass. Briefly, WC (60.00 g) was suspended with copper(II) nitrate trihydrate ($Cu(NO_3)_2 \cdot 3H_2O$; 11.41g) in deionized water (300 mL). The resulting slurry was agitated at 500 rpm for 1 h, followed by oven-drying (95 ˚C) for 72 h. For a comparison, pristine WC was prepared by the same procedure in the absence of the Cu. Thermochemical treatment was performed in a quartz tubular reactor (22 mm inner diameter, 25 mm outer diameter, 1000 mm length) and an electrically heated cylindrical furnace. The reactor was fastened at both ends using hermetically tight connections (SS-4-UT-6-600, Swagelok, USA). A fixed mass (10.00 ± 0.01 g) of WC or Cu-impregnated WC was placed in the reactor at the middle of the heating area. The temperature of the heating area was

increased up to 700 ˚C from 100 ˚C at 10 ˚C $min^{-1}$ and held at 700 ˚C for 1 h. The total gas flow rate of 800 mL $min^{-1}$ was fixed throughout the experiment. Under $N_2$ conditions, $N_2$ was supplied at 800 mL $min^{-1}$, whereas under $CO_2$ the mixed gas stream composed of 640 mL $min^{-1}$ $CO_2$ and 160 mL $min^{-1}$ $N_2$ was supplied. The resulting biochars were denoted as WCB ($N_2$), WCB ($CO_2$), CuWCB ($N_2$), and CuWCB ($CO_2$), respectively. The recovered biochars were subsequently ball-milled prior to further experiments.

**Recovery and analysis of bio-oil compounds and gases**

During thermochemical treatment of WC, liquid, and gaseous products were obtained. The condensable fraction was recovered as bio-oil using a condensation system with a coolant maintained at -40 ˚C. The collected bio-oil was diluted with a methanol/dichloromethane mixture (150 mL each) prior to analysis and characterized by gas chromatography-mass spectrometry (GC-MS; 8890-5997B, Agilent, USA) fitted with a DB-WAX capillary column (30 m × 250 μm × 0.25 μm). Non-condensable gaseous products were continuously withdrawn from the reactor outlet and analyzed online using a micro-gas chromatography (micro-GC; INFICON 3000A, Switzerland) equipped with a molecular sieve 5A packed column (10 m × 320 μm × 30 μm) and a PLOT U capillary column (8 m × 320 μm × 30 μm). The concentrations of gaseous species, including $H_2$, CO, $CH_4$, $C_2H_2$, $C_2H_4$, and $C_2H_6$, were quantified to assess the evolution of product gas composition and the extent of syngas generation.

**Characterizations of WC and biochars**

The morphologies of WCBs and CuWCBs samples were examined using transmission electron microscopy (TEM, JEM-2100F, JEOL, Japan). Surface functional groups were identified using Fourier-transform infrared (FT-IR) spectroscopy (Cary 630, Agilent, USA) over 650-4000 $cm^{-1}$. Surface chemical states of the catalysts were characterized by X-ray photoelectron spectroscopy (XPS; K-Alpha+, Thermo

Scientific, UK) using a monochromated X-ray source. Binding energy scale was corrected by referencing the C 1s signal to 284.6 eV. Crystalline phases were characterized by X-ray diffraction (XRD) using an X-ray diffractometer (Empyrean, PANalytical, Netherlands) equipped with a 4 kW X-ray generator and Cu Kα radiation. Diffraction patterns were acquired in the 2θ range of 5-90˚ with a 0.026˚ step. $N_2$ adsorption-desorption isotherm measurements were performed using a Brunauer-Emmett-Teller (BET) surface area analyzer (Belsorp-max II, MicrotracBEL, Japan). Prior to analysis, all biochars were degassed under vacuum at 250 ˚C for 2 h to remove adsorbed moisture and gases. Pore size distributions were derived using the Barrett-Joyner-Halenda (BJH) method from the adsorption branch. Micropore volume ($V_{MP}$) was determined using the t-plot method. Thermogravimetric analysis (TGA) of WC and Cu-impregnated WC was evaluated using a thermogravimetric analyzer (STA 449 F5 Jupiter, Netzsch, Germany). 10.0 ± 0.1 mg of samples were loaded into an alumina crucible and heated from 40 to 900 ˚C at a heating rate of 10 ˚C $min^{-1}$. Measurements were conducted under $N_2$ and $CO_2$ with a total gas flow rate of 100 mL $min^{-1}$. For the $CO_2$ atmosphere, $CO_2$ was supplied at a flow rate of 80 mL $min^{-1}$, with $N_2$ (20 mL $min^{-1}$) used as a safety purge gas. Electron paramagnetic resonance (EPR) spectrum was recorded using an EPR spectrometer (EMXplus, Bruker, USA). TEMP (2,2,6,6-tetramethylpiperidine, 20 mM) was used as a spin-trapping agent, and the samples were collected 3 min after PDS addition.



**Adsorption and PDS activation experiments**

The adsorption performance and PDS-activation capability of WCBs and CuWCBs were evaluated by BPA removal efficiency. Each run comprised an adsorption stage (0-40 min) followed by a PDS oxidation stage (40-70 min). PDS (1 mM) was added to 40 mL of the catalyst suspension (0.4 g $L^{-1}$) containing BPA (70 μM). Reaction aliquots were collected every 10 min over a 70 min period, filtered, and then analyzed for BPA concentration. Scavenger tests were performed by adding MeOH (100 mM), CF (1 mM), or SA

(1 mM). The involvement of Cu sites in PDS activation was probed using sodium thiocyanate (NaSCN, 1 mM) as a complexing agent.

**Analytical methods**

BPA concentrations were quantified using high-performance liquid chromatography (HPLC, Agilent 1200 Series) equipped with a quaternary pump (G1311A), vacuum degasser (G1322A), autosampler (G1329A), column oven (G1316A), and variable-wavelength detector (G1314B). BPA was separated on a reversed-phase C18 column using an isocratic elution with a DI water/ACN (55:45, v/v) mobile phase at 1.0 mL $min^{-1}$. The column was thermostated at 35 ˚C, and a 5 µL aliquot was injected. BPA was monitored at 230 nm. The concentration of benzoic acid (BA) and 4-hydroxybenzoic acid (4-HBA) was quantified at isocratic mobile phase of water containing 0.1% formic acid/acetonitrile (80:20, v/v) with UV detection at 254 nm. The Cu concentration in the solution was quantified by inductively coupled plasma optical emission spectrometry (ICP-OES; 5800, Agilent, USA).

**Electrochemical analysis**

Electrochemical measurements were conducted using a potentiostat (CompactStat, Ivium) with a three-electrode setup consisting of a biochar-coated FTO working electrode, a platinum wire counter electrode, and an Ag/AgCl (saturated KCl) reference electrode. All measurements were performed in 40 mL of 0.5 M $Na_2SO_4$ aqueous electrolyte (pH 6.5). The working electrode ink was prepared by dispersing 4 mg of biochar in 1 mL of an ethanol/DI water mixture (2:3, v/v) containing Nafion (10 µL) and sonicated for 30 min to obtain a homogeneous ink. 150 µL of the ink was coated onto a pre-cleaned fluorine-doped tin oxide glass substrate (1.0 cm × 2.0 cm) and dried at 75 ˚C. Open-circuit potential (OCP) measurements were recorded after 2 min of baseline, followed by the addition of 200 µL of PDS (100 mM). After stabilization of the OCP (± 1 mV $min^{-1}$), 1 mL of BPA solution (1 mM) was introduced.

Chronoamperometry (CA) measurements were performed following the identical dosing sequence as the OCP measurement. Electrochemical impedance spectroscopy (EIS) measurements were performed over 0.1-$10^5$ Hz.

## Data availability

The datasets generated and/or analyzed during the current study are not publicly available due to ongoing follow-up analyses but are available from the corresponding author on reasonable request.

## Acknowledgements

This work was supported by the National Research Foundation of Korea (NRF) grants funded by the Korean Government (MSIT) (Grant No. RS-2023-NR077231 and RS-2025-00556963).

## Author contribution

C.Y.: Writing original draft, reviewing, conceptualization, data curation & Investigation, and editing. Y-J.L.: Writing original draft, data curation & Investigation. S-J.P.: Writing original draft and reviewing. D.L.: Writing original draft, reviewing, conceptualization, supervision, and funding. E.E.K.: Writing original draft, reviewing, conceptualization, supervision, and funding. All authors have read and approved the manuscript.



## Competing interest

The authors declare no competing financial or non-financial interests.

## References


1. Al-Tohamy R*, et al.* A critical review on the treatment of dye-containing wastewater: Ecotoxicological and health concerns of textile dyes and possible remediation approaches for environmental safety. *Ecotoxicology and Environmental Safety* **231**, 113160 (2022).

2. Rashid R, Shafiq I, Akhter P, Iqbal MJ, Hussain M. A state-of-the-art review on wastewater treatment techniques: the effectiveness of adsorption method. *Environmental Science and Pollution Research* **28**, 9050–9066 (2021).

3. Xiang Y*, et al.* Carbon-based materials as adsorbent for antibiotics removal: Mechanisms and influencing factors. *Journal of Environmental Management* **237**, 128–138 (2019).

4. Yuan J, Passeport E, Hofmann R. Understanding adsorption and biodegradation in granular activated carbon for drinking water treatment: A critical review. *Water Research* **210**, 118026 (2022).

5. Parniske J, Froemelt A, Morck T. Modelling competitive adsorption of organic micropollutants onto granular activated carbon in fixed-bed adsorbers for advanced wastewater treatment. *Water Research* **288**, 124631 (2026).

6. Mangla D, Annu, Sharma A, Ikram S. Critical review on adsorptive removal of antibiotics: Present situation, challenges and future perspective. *Journal of Hazardous Materials* **425**, 127946 (2022).

7. Liu Y, Zhao Y, Wang J. Fenton/Fenton-like processes with in-situ production of hydrogen peroxide/hydroxyl radical for degradation of emerging contaminants: Advances and prospects. *Journal of Hazardous Materials* **404**, 124191 (2021).

8. Ye F*, et al.* Construction of adsorption-oxidation bifunction-oriented carbon by single boron doping for non-radical antibiotic degradation via persulfate activation. *Chemical Engineering Journal* **454**, 140148 (2023).

9. Pan Y, Meng F, Bai J, Song B, Cao Q. Highly efficient peroxymonosulfate activation by $CoFe_2O_4$@attapulgite–biochar composites: Degradation properties and mechanism insights. *Journal of Environmental Chemical Engineering* **12**, 112579 (2024).

10. Chu C*, et al.* Cooperative Pollutant Adsorption and Persulfate-Driven Oxidation on Hierarchically Ordered Porous Carbon. *Environ Sci Technol* **53**, 10352–10360 (2019).

11. Jiang Q*, et al.* Graphene-like carbon sheet-supported nZVI for efficient atrazine oxidation degradation by persulfate activation. *Chemical Engineering Journal* **403**, 126309 (2021).

12. Jiang Q, Jiang S, Li H, Zhang R, Jiang Z, Zhang Y. A stable biochar supported S-nZVI to activate persulfate for effective dichlorination of atrazine. *Chemical Engineering Journal* **431**, 133937 (2022).

13. Huang P, Zhang P, Wang C, Tang J, Sun H. Enhancement of persulfate activation by Fe-biochar composites: Synergism of Fe and N-doped biochar. *Applied Catalysis B: Environmental* **303**, 120926 (2022).

14. Zhao C*, et al.* Activation of peroxymonosulfate by biochar-based catalysts and applications in the degradation of organic contaminants: A review. *Chemical Engineering Journal* **416**, 128829 (2021).

15. Luo H, Fu H, Yin H, Lin Q. Carbon materials in persulfate-based advanced oxidation processes: The roles and construction of active sites. *Journal of Hazardous Materials* **426**, 128044 (2022).

16. Pan X, Gu Z, Chen W, Li Q. Preparation of biochar and biochar composites and their application in a Fenton-like process for wastewater decontamination: A review. *Science of The Total Environment* **754**, 142104 (2021).

17. Zhang S, Wang J, Ye L, Li S, Su Y, Zhang H. Investigation into biochar supported Fe-Mo carbides catalysts for efficient biomass gasification tar cracking. *Chemical Engineering Journal* **454**, 140072 (2023).

18. Wu W*, et al.* Hierarchical pore structure engineering in bamboo shoot sheath-derived biochar: Synergistic effects of bio-templated chemical activation and gradient pyrolysis. *Journal of Analytical and Applied Pyrolysis* **193**, 107466 (2026).

19. Mustafa FS, Hama Aziz KH. Heterogeneous catalytic activation of persulfate for the removal of rhodamine B and diclofenac pollutants from water using iron-impregnated biochar derived from the waste of black seed pomace. *Process Safety and Environmental Protection* **170**, 436–448 (2023).

20. Pan X, Wang X, Liu L, Kuang S, Zheng H. $CO_2$ and $H_2O$ as sweep gases elevated carbon stability and decreased phytotoxicity of biochars. *Chemical Engineering Journal* **472**, 145035 (2023).

21. Parthasarathy P, Zuhara S, Al-Ansari T, McKay G. A review on catalytic $CO_2$ pyrolysis of organic wastes to high-value products. *Fuel* **335**, 127073 (2023).

22. Akın SŞ, Kır AB, Kazanc F. Impact of nitrogen and alkali dopants on pore architecture and surface functionalities of biochar in one-step $CO_2$ pyrolysis. *Journal of Analytical and Applied Pyrolysis* **186**, 106962 (2025).

23. le Saché E, Reina TR. Analysis of Dry Reforming as direct route for gas phase $CO_2$ conversion. The past, the present and future of catalytic DRM technologies. *Progress in Energy and Combustion Science* **89**, 100970 (2022).

24. Qi F*, et al.* Strong metal-support interaction (SMSI) in environmental catalysis: Mechanisms, application, regulation strategies, and breakthroughs. *Environmental Science and Ecotechnology* **22**, 100443 (2024).

25. Dong L*, et al.* Mechanism of biochar-Cu-based catalysts construction and its electrochemical $CO_2$ reduction performance. *Carbon Capture Science & Technology* **13**, 100250 (2024).

26. Wan Z*, et al.* A sustainable biochar catalyst synergized with copper heteroatoms and CO2 for singlet oxygenation and electron transfer routes. *Green Chemistry* **21**, 4800–4814 (2019).

27. Cuong DV*, et al.* A critical review on biochar-based engineered hierarchical porous carbon for capacitive charge storage. *Renewable and Sustainable Energy Reviews* **145**, 111029 (2021).

28. Yang X, Cheng J, Yang X, Xu Y, Sun W, Zhou J. MOF-derived Cu@$Cu_2O$ heterogeneous electrocatalyst with moderate intermediates adsorption for highly selective reduction of $CO_2$ to methanol. *Chemical Engineering Journal* **431**, 134171 (2022).

29. Dong W*, et al.* Hydrogen bonds between the oxygen-containing functional groups of biochar and organic contaminants significantly enhance sorption affinity. *Chemical Engineering Journal* **499**, 156654 (2024).

30. Jang J*, et al.* Facile design of oxide-derived Cu nanosheet electrocatalyst for $CO_2$ reduction reaction. *EcoMat* **5**, e12334 (2023).

31. Zhang B*, et al.* Highly Electrocatalytic Ethylene Production from $CO_2$ on Nanodefective Cu Nanosheets. *Journal of the American Chemical Society* **142**, 13606–13613 (2020).

32. Boruban C, Esenturk EN. Activated carbon-supported CuO nanoparticles: a hybrid material for carbon dioxide adsorption. *Journal of Nanoparticle Research* **20**, 59 (2018).

33. Mei Y, Xu J, Zhang Y, Li B, Fan S, Xu H. Effect of Fe–N modification on the properties of biochars and their adsorption behavior on tetracycline removal from aqueous solution. *Bioresource Technology* **325**, 124732 (2021).

34. Long H*, et al.* Adsorption and diffusion characteristics of $CH_4$, $CO_2$, and $N_2$ in micropores and mesopores of bituminous coal: Molecular dynamics. *Fuel* **292**, 120268 (2021).

35. Zhao Z*, et al.* Regulating nonradicals generation through peroxymonosulfate activation via localized dipole to enhance wastewater biodegradability. *Nature Communications* **16**, 5861 (2025).

36. Zheng W*, et al.* Sustainable Generation of Sulfate Radicals and Decontamination of Micropollutants via Sequential Electrochemistry. *Engineering* **30**, 144–152 (2023).

37. Liu J, Ding C, Gong S, Fu K, Deng H, Shi J. Enhanced Degradation of Antibiotic by Peroxydisulfate Catalysis with CuO@CNT: Simultaneous $^1O_2$ Oxidation and Electron-Transfer Regime. *Molecules* **27**, 7064 (2022).

38. Koundle P, Nirmalkar N, Momotko M, Makowiec S, Boczkaj G. Tetracycline degradation for wastewater treatment based on ozone nanobubbles advanced oxidation processes (AOPs) – Focus on nanobubbles formation, degradation kinetics, mechanism and effects of water composition. *Chemical Engineering Journal* **501**, 156236 (2024).

39. Wang H, Gao L, Xie Y, Yu G, Wang Y. Clarification of the role of singlet oxygen for pollutant abatement during persulfate-based advanced oxidation processes: $Co_3O_4$@CNTs activated peroxymonosulfate as an example. *Water Research* **244**, 120480 (2023).

40. Joo SH, Feitz AJ, Sedlak DL, Waite TD. Quantification of the Oxidizing Capacity of Nanoparticulate Zero-Valent Iron. *Environmental Science & Technology* **39**, 1263–1268 (2005).

41. Laschuk NO, Easton EB, Zenkina OV. Reducing the resistance for the use of electrochemical impedance spectroscopy analysis in materials chemistry. *RSC Advances* **11**, 27925–27936 (2021).

42. Lazanas AC, Prodromidis MI. Electrochemical Impedance Spectroscopy—A Tutorial. *ACS Measurement Science Au* **3**, 162–193 (2023).

43. Zhu Y*, et al.* $Cu_2O$/CuO induced non-radical/radical pathway toward highly efficient peroxymonosulfate activation. *Journal of Environmental Chemical Engineering* **9**, 106781 (2021).

44. Xie J, Pan X, Jiang C, Zhao L, Gong X, Liu Y. Enhanced conversion of superoxide radical to singlet oxygen in peroxymonosulfate activation by metal-organic frameworks derived heteroatoms dual-doped porous carbon catalyst. *Environmental Research* **236**, 116745 (2023).

45. Li F*, et al.* Self-dispersed Fe single-atom anchored biochar derived from hyperaccumulator residues with intrinsic Zn and Fe for selective peroxymonosulfate activation via electron transfer process. *Chemical Engineering Journal* **482**, 149052 (2024).

46. Wang N, Lin C, Ren Z, Xu Q, Wang S. Radical and non-radical mechanisms for removal of micropollutants in peroxymonosulfate activation systems: Their generation and identification. *Applied Catalysis B: Environment and Energy* **383**, 126139 (2026).

47. Liu S*, et al.* Enhanced Mediated Electron Transfer Pathway of Peroxymonosulfate Activation Dominated with Graphitic-N for the Efficient Degradation of Various Organic Contaminants in Multiple Solutions. *ACS ES&T Water* **2**, 817–829 (2022).

48. Xiao C*, et al.* Degradation of sulfamethoxazole by super-hydrophilic $MoS_2$ sponge co-catalytic Fenton: Enhancing $Fe^{2+}$/$Fe^{3+}$ cycle and mass transfer. *Journal of Hazardous Materials* **458**, 131878 (2023).

49. Xiao C, Li X, Li Q, Hu Y, Cheng J, Chen Y. Ni-doped $FeC_2O_4$ for efficient photo-Fenton simultaneous degradation of organic pollutants and reduction of Cr(VI): Accelerated Fe(III)/Fe(II) cycle, enhanced stability and mechanism insight. *Journal of Cleaner Production* **340**, 130775 (2022).

50. Xiao C*, et al.* Carbon-doped defect $MoS_2$ co-catalytic $Fe^{3+}$/peroxymonosulfate process for efficient sulfadiazine degradation: Accelerating $Fe^{3+}$/$Fe^{2+}$ cycle and $^1O_2$ dominated oxidation. *Science of The Total Environment* **858**, 159587 (2023).

51. Xiang Y*, et al.* Rapid and efficient removal of organophosphorus pollutant and recovery of valuable elements: A boosted strategy for eliminating organophosphorus from wastewater. *Water Research* **267**, 122494 (2024).

52. Brebu M, Ioniță D, Stoleru E. Thermal behavior and conversion of agriculture biomass residues by torrefaction and pyrolysis. *Scientific Reports* **15**, 11505 (2025).

53. Wang J*, et al.* $CO_2$ Hydrogenation to Methanol over $In_2O_3$-Based Catalysts: From Mechanism to Catalyst Development. *ACS Catalysis* **11**, 1406–1423 (2021).

54. Hong J*, et al.* Copper-catalyzed pyrolysis of halloysites@polyphosphazene for efficient carbonization and smoke suppression. *Composites Part B: Engineering* **230**, 109547 (2022).

55. Koul B, Yakoob M, Shah MP. Agricultural waste management strategies for environmental sustainability. *Environmental Research* **206**, 112285 (2022).

56. Deng W*, et al.* Catalytic conversion of lignocellulosic biomass into chemicals and fuels. *Green Energy & Environment* **8**, 10–114 (2023).

57. Qiu B, Tao X, Wang J, Liu Y, Li S, Chu H. Research progress in the preparation of high-quality liquid fuels and chemicals by catalytic pyrolysis of biomass: A review. *Energy Conversion and Management* **261**, 115647 (2022).